RSC Advances

ROYAL SOCIETY
OF CHEMISTRY

www.rsc.org/advances

On-chip integration of novel Au electrode with a higher order three-dimensional layer stack nanostructure for surface-enhanced Raman spectroscopy

Akinobu Yamaguchi*, Takao Fukuoka, Ryohei Hara, Kazuhisa Kuroda, Ryo Takahashi and Yuichi Utsumi

Laboratory of Advanced Science and Technology for Industry, University of Hyogo, 3-1-2 Koto, Kamigori, Hyogo 678-1205, JAPAN

Abstract

Highly sensitive surface-enhanced Raman spectroscopy (SERS) with additional functionality has recently attracted growing interest; however, it has been demonstrated experimentally in only a few microscopic systems. Here, we develop a novel SERS platform with three-dimensional nanostructure gold electrodes using the competitive self-assembly between dielectrophoresis and convective aggregation. Appropriate conditions are able to provide the gold electrode with a higher order nanostructure to achieve in situ highly sensitive SERS of analytes. As such, our approach could enable the development of active functional control devices for in situ SERS.

I.   Introduction

Recently, surface-enhanced Raman scattering (SERS) has attracted much attention due to its fundamental chemical and molecular science and potential applications in medical diagnosis and environmental analysis, *etc*.[1-6] Single molecule detection has also been demonstrated.[3, 4] SERS detection has mainly been achieved with colloidal nanoparticles. The junctions generated between colloidal nanoparticles are capable of generating large enhancements in electromagnetic fields, boosting the Raman signal originating from the molecular sample. However, the poor structural reproducibility and instability of the SERS-active nanoscale junctions are remained in SERS measurement using colloidal nanoparticles, which poses significant issues. Many novel nanojunctions have been proposed and demonstrated to solve these issues using oxide shell–isolated nanoparticles (including nanoshells)[5-9], nanoporous substrates[10, 11] and substrates nanofabricated through a combination of bottom–up and top–down processes to form the nanoscale junctions between nanostructures.[12-16] In addition, in situ SERS detection has recently been reported in microfluidic devices, [17, 18] which compensate for these issues and achieve a micro total analysis system and lab on a chip for food analysis and medical diagnostics. Such systems also allow for high–throughput analysis with high precision.

Beyond the SERS platforms described above, control and measurement of molecules and analytes have been recently studied. An attractive aspect of in situ SERS with an external input, such as dielectrophoresis, [19-22] an electric field[23] or magnetic field, [24] is that the Raman spectral scattering can be tracked in real time by changing the external input. Several groups have demonstrated the in situ dynamic measurement of the SERS signal using an optoelectrofluidic SERS platform.[19] Adding functionality with an external input to actual SERS platforms would be extremely challenging as even a single molecule can be directly controlled and measured the electronic states measured with respect to the external input. On–chip integration is therefore necessary for the development of several applications. Moreover, this platform could eventually yield fundamental performance advantages over macroscopic experiments. For example, nanopatterned objects can have a significantly higher surface to volume ratio, providing reaction sites for chemical and physical reactions.

Herein we present the design, realization, and characterization of a novel electrode with a higher order nanostructure through integration of a three–dimensional Au structure, achieving SERS detection of molecules.

II. Concept and principle

4

A. In situ SERS platform device

Figure 1 depicts the in situ SERS platform which possesses dielectrophoresis control

due to the higher–order three–dimensional nanostructure gold electrodes. Our basic idea

was that dielectrophoresis would be able to control the colloidal particles and

aggregation of the three–dimensional nanostructure at the desired position on demand.

Figure 2 shows a schematic of the fabrication process using a mixture of metallic

nanoparticles and polystyrene (PS) nanoparticles manipulated by the dielectrophoretic

(DEP) force. First, we prepared the pair of electrodes and a well to contain the solution

[Fig. 2(a)]. Following addition of the solution, dielectrophoresis was induced by the

application of an alternating current (AC) to cause aggregation and construct the

higher–order three–dimensional layer stack nanostructure consisting of gold

nanoparticles (AuNPs) and PS [Fig. 2(b)]. Figure 2(c) shows the schematic of structural

formation under the competition of aggregation and evaporation of the solution. After

evaporation, the higher–order layer stack three dimensional nanostructure, including

both AuNPs and PS particles, was formed as shown schematically in Fig. 2(d). Finally,

to remove PS after peeling off the poly(dimethylsiloxane) (PDMS) sheet, the assembled

higher–order nanostructure was soaked in dichloromethane. We then obtained the novel

electrode mounted with the higher–order nanostructure, as shown in Fig. 2(e).

B. Formation mechanism of higher–order nanostructure

The mechanism of formation of the higher–order layer stack nanostructure is described

by the competitive self-assembly[14-16)] between radial flow, Marangoni recirculating flow,

Derjaguin, Landau, Verway and Overbeek (DLVO) interactions and sedimentation

under dielectrophoresis. Here, accordingly to DLVO theory[25-29)], the interaction free

energy potential between two hetero spheres is described by

$$U = \frac{\varepsilon_r \varepsilon_0 R_1 R_2}{4(R_1 + R_2)} \cdot \left[2\psi_1 \psi_2 \left\{ \frac{1 + \exp(-\kappa d)}{1 - \exp(-\kappa d)} \right\} + (\psi_1^2 + \psi_2^2) \ln\{1 - \exp(-2\kappa d)\} \right] - \frac{A_{132} R_1 R_2}{6(R_1 + R_2)d}, \quad (1)$$

where ε_r and ε_0 are the relative permittivity of water and the permittivity of a

vacuum, respectively, and ψ_1 and ψ_2 denote the zeta potentials of spheres 1 and 2,

respectively. Here, zeta potentials of AuNPs and PS are assumed to be -46.12 and -41.16

mV, respectively. The radii of AuNPs and PS are 20 and 300 nm, respectively. The

Debye screening length Hamaker constant are represented by $1/\kappa$ and A_{132},

respectively. Here, the Hamaker constant (A_{132}) represents the interaction between

media 1 and 2 through medium 3.

Figures 3(a) – 3(c) show the DLVO interaction free potential energies as a

function of distance between the particles; PS–PS, PS–AuNP and AuNP–AuNP,

respectively. The inset of Fig. 3(a) represents the analytical model of DLVO interaction

6

between hetero particles. All calculations were derived from Eq. (1). The forces

between the particles was calculated by the differential potential; i. e. $F = -\partial U/\partial x$,

where U and x denote the potential and coordinate axis, respectively. Figures 3(d) –

3(f) display the forces exerted on the particles as a function of the distance.

Next, we evaluate the higher–order stack layer nanostructure deposition

process onto the electrode and substrate using the similar procedure described in our

previous study.[16] Here, under the assumption that a particle with a spherical radius R

stays aloof at a height h between the particle and glass substrate, the interaction free

energy between the particle and substrate is given by[25 – 29]

$$U = \pi\varepsilon_r\varepsilon_0 R \left[2\psi_P\psi_S \left\{\frac{1 + \exp(-\kappa h)}{1 - \exp(-\kappa h)}\right\} + (\psi_P^2 + \psi_S^2)\ln\{1 - \exp(-2\kappa h)\}\right]$$

$$- \frac{A_{132}R}{6h}[1 + (14\kappa h)]^{-1}, \tag{2}$$

where ψ_P and ψ_S denote the zeta potentials of the particle and substrate, respectively.

Here, zeta potential of glass substrate and Au electrode are adopted to be -66 mV[30] and

-46.12 mV, respectively. To simplify the calculation, we estimate the calculated

potential energies of AuNP–glass substrate and PS–glass substrate are plotted as a

function of height h in Figs. 4(a) and 4(b), respectively. The forces between particle and

substrate can be calculated by differential potential, that is $F = -\partial U/\partial z$. Figures 4(c)

and 4(d) show the height dependence of the force between particle and substrate. In the

similar way, Figures 5(a) and 5(b) display the potential energies as a function of height

h for the cases of (a) AuNP–Au electrode and (b) PS–Au electrode, respectively. The

forces calculated by the respective potential energies (AuNP– and PS–Au electrode) are

plotted as shown in Figs. 5(c) and 5(d), respectively. As shown in these evaluation

results, the DLVO repulsion force prevent the deposition of the particles onto the Au

electrode and glass substrate. Here, a particle traveling in a droplet experiences not only

DLVO interactions but also other forces. In the vertical direction, hydrodynamic from

radial flow and Marangoni flow, sedimentation and DEP forces act to determine the

particle height in the fluidic flow profile. Here, we consider the equilibrium, which is

the sedimentation dominating the deposition of particles.

The sedimentation of spherical particle under the constant flow in equilibrium

is described by[31]

$$\frac{\partial \boldsymbol{u}}{\partial t} = \frac{\sigma - \rho}{\sigma + \rho/2} g, \tag{3}$$

where $\boldsymbol{u}$ is velocity vector of the particle, that is $\partial \boldsymbol{u}/\partial t$ represents the acceleration. σ

and ρ are mass densities of particle and media, respectively. g is the acceleration due

to gravity, that is 9.8 m/s². Here, the mass densities of Au, PS and water are 19.3×10^3,

1050 and 997 kg/m³, respectively. Substituting these densities into Equation (3), the

gravitation forces working AuNP and PS are estimated to about 5.86×10^{-18} and

3.98×10^{-17} N, respectively. The gravitation forces working AuNP and PS are always

larger than the DLVO repulsion forces between particles and substrate. Thus, we show

the sedimentation enables us to deposit the particles onto the substrate and Au electrode.

Finally, we present that DEP force can control the deposition of particles in a

more aggressive manner. The DEP force exerted on particles with diameter a is given

by:[32-34]

$$F_{\text{DEP}} = 2\pi a^3 \epsilon_m \text{Re}[f_{\text{CM}}] \nabla |E|^2, \tag{4}$$

where ϵ_m and $\text{Re}[f_{\text{CM}}]$ are the permittivity of the medium and real part of the

Clausius–Mossotti factor, respectively. Here, we estimate each Clausius–Mossotti factor

under the low frequency limit as the applied AC electric field was ~ 100 kHz, which is

almost considered to be a direct current (DC) field. The frequency–dependent complex

permittivity can be treated as the conductivity; therefore, we assumed that $\text{Re}[f_{\text{CM}}] = 1$.

We used deionized water with a permittivity of $\epsilon_m = 80\epsilon_0 = 80 \times 8.85 \times 10^{-12}$

[F/m] and $\sigma_m = 5.5$ [μS/m]. To evaluate the DEP force by varying the particle radius,

the medium and AC electric field were fixed. Figure 6 shows the particle radius

dependence of the DEP force on 50, 100 and 150 μm electrode widths and gaps.

By comparison of the DEP, DLVO interaction and sedimentation forces, we

found that the DEP force manipulating the AuNPs and PS particles was larger than the

DLVO repulsive forces between particles located away from each other. Thus the DEP

forces cause the collection of the particles on the electrode by overcoming the DLVO

repulsive force. The closer the particles come to each other, the larger the van der Waals

attractive forces become. The AuNPs can then infiltrates the gaps between PS particles,

forming aggregates. Therefore, formation of the higher–order layer stack nanostructure

is caused by colloidal particle deposition resulting from the competition among

sedimentation[16], radial flow, Marangoni flow, DLVO interactions and DEP force, as

shown in Fig. 2. In particular, the DEP force can actively trigger the formation of a

higher–order laminar nanostructure with AuNPs and PS particles. As shown in Fig. 2,

the DEP force enables us to control and coagulate the higher–order nanostructure at our

desired position on demand. Here, we demonstrate the novel electrode with a higher–

order layer stack Au nanostructure, as shown in Fig. 2(d).

III. Experimental methods

A. Preparation of the Au and polystyrene beads

Au colloids with 20 nm diameters were prepared according to the standard citrate

reduction method reported by Lee and Meisel.[35] The AuNP dispersion was prepared at

0.48 mM. Polystyrene latex beads (PS) with 600 nm diameters (Invitrogen Inc., 8%

w/v) were concentrated by centrifugation and washed to yield a 10 % w/v suspension.[15,][16)] The concentration of AuNPs and PS were estimated to be 1.17×10^{15} and 8.42×10^{14} particles/L, respectively. AuNPs were concentrated 50–fold by centrifuging at 12000 rpm for 15 min twice with one extraction. AuNPs were mixed with PS to prepare various ratios of (i) 700 : 1, (ii) 1000 : 1 and (iii) 1300 : 1 (AuNP : PS).

B. Preparation of the electrode

A schematic of the electrodes for dielectrophoresis is shown in Fig. 7, with two circular electrodes arranged in a concentric pattern. These electrodes were fabricated on glass slides (Matsunami Glass Ind., Ltd.) by means of standard UV lithography and the lift–off technique. The electrodes prepared from Au (80 nm)/Cr (5 nm) were connected to an arbitrary function generator (Keysight technology, 33510B). We designed the circular electrode with 50, 100 and 150 μm widths and gaps, as this shape enabled us to control the AuNPs and PS particles through dielectrophoresis.

C. Preparation of the system

A silicone sheet with a through hole with 6 mm diameter was placed on an ultraviolet–

cleaned glass slide, where the Au electrodes were previously fabricated, and a well was formed. The mixed solution (38 µL) of AuNPs and PS was placed in the well and covered with a cover glass to prevent the droplet from drastically evaporating.

IV. Results and discussion

A. Evaluation of the electrode

Here, we simultaneously applied an AC electric field of 1 to 100 kHz to various concentration of PS and AuNPs in the vicinity of the electrodes. The PS and AuNPs irreversibly formed aggregates and the DEP force did not enable dynamic control of the aggregation and disaggregation. When the maximum number of particles were irreversibly immobilized, the structure was soaked in dichloromethane to remove the PS. All experimental conditions are summarized in Table 1. The higher order nanostructure was successfully obtained under several conditions. Figure 7(b) shows the optical photograph of the top view of the whole system after forming the nanostructure under condition #9. Scanning electron microscope (SEM) images are displayed in Figs. 7(c) and 7(d), showing that the formed higher–order layer stack nanostructure was connected to the outer electrode.

Under condition #12, the higher–order layer stack nanostructure could be

mounted on the outer electrode, as shown in Fig. 8. The magnified SEM images [Figs.

8(b) and 8(c)] demonstrate that the width of the entire nanostructure was approximately

30 – 40 μm in the radial direction. The higher resolution SEM image [Fig. 8(d)]

revealed the formation of a higher–order porous layer stack nanostructure consisting of

AuNPs. The two dimensional–like nanostructure was formed under condition #21, as

shown in Fig. 9. We found that we were able to fabricate a higher–order nanostructure

under only three conditions: #9, #12 and #21. The summary shown in Table 1 indicates

that we are able to obtain the electrode with the higher–order layer stack nanostructure

only when the ratio of Au : PS was 1300 : 1, as this provides the quantity of AuNPs

required for the conservation of the higher–order nanostructure after the removal of PS.

By applying AC fields of 1 and 100 kHz, the particles gathered on the middle and outer

side of the outer electrode, respectively. Au electrode with of 50 μm is not considered to

be wide enough to form and conserve the higher–order nanostructure. This is why

condition #3 could not form the higher–order nanostructure even with the appropriate

ratio of Au : PS.

Conversely, the higher–order layer stack nanostructure was formed on the outer

side of the outer electrode only under condition #9. This is attributable to the narrow

spatial electric field distribution realized on the outer side of the outer electrode. A pearl

chain structure appeared under most conditions, as shown in Fig. 10. This is attributable

to the migration of AuNPs as a result of dielectrophoresis. Formation of the pearl chain

caused by the DEP force induced a deficiency in AuNPs required for the formation of

the higher–order nanostructure. In addition, the pearl chain also induced a circulatory

shunt between the electrodes and stops the dielectrophoresis, consequently the pearl

chain prevented the aggregation of particles. In our experiment, the ratio of AuNPs :

PSs suitable to building the higher–order layer stack nanostructure is expected to be

occasionally 1300 : 1. The procedure for the construction of our device is reproducible

under the condition which prevent the solution from spilling.

Thus, the dielectrophoresis–enabled formation of the higher–order or pearl

chain nanostructure was achieved on some level. These nanostructures have the ability

to improve surface–enhanced Raman scattering spectroscopy, battery cells, photovoltaic

cells, *etc*.

B. Photoluminescence measurement

To evaluate the properties of novel Au electrode with higher–order AuNPs layer

stack structure, we measured photoluminescence (PL) spectroscopy of the

nanostructure and flat Au electrode using the NRS-5100 (JASCO) system. The 532

nm Green laser was used to excite the PL. Figure 11 shows the PL intensity spectra

of Au electrode (a) with and (b) without the higher–order AuNPs layer stack structure.

The inset of optical photograph display the measurement positions. As shown in Fig.

11, the large enhancement of the PL spectra from the Au electrode with the higher–

order AuNPs layer stack structure is revealed. This result indicates that the higher–

order AuNPs layer stack structure can provide electric field enhancement.

C. SERS measurement

We demonstrated the *in situ* SERS measurement of 4,4′-bipyridine (4bpy) as a Raman

active molecule using the prepared higher–order layer stack gold nanostructure on the

electrode formed under condition #12. The silicone sheet with a 6 mm–diameter

through hole was placed on the higher order layer stack gold nanostructure on the glass

to enable good accurate measurement.[15, 16, 22] An aqueous 4bpy solution (35 µL) with a

various concentration was dropped into the well on the higher–order layer stack gold

nanostructure. A cover glass was used to prevent the 4bpy solution from evaporating

and to maintain its concentration. The higher order layer stack gold nanostructure was

placed in the simple Raman spectrometer without microscope (RAM–100S, Lambda

Vision Inc.), and a 785 nm wavelength laser (laser power, 50 mW) was used to irradiate

the higher order layer stack gold nanostructure for 1 s.

The higher–order layer stack nanostructure enabled us to detect concentrations below 100 nM 4bpy as shown in Fig. 12. Through comparison of all spectra plotted in Fig. 12, the characteristic enhanced Raman spectra of 4bpy (characteristic peak positions at 1000, 1250, and 1582 cm^{-1}) were clearly observed.[36] To compare the SERS–activity of flat Au electrode and Au electrode with the higher–order nanostructure, we display the SERS spectrum of 10 mM 4bpy using the flat Au electrode. We afresh confirm the enhancement of SERS–activity induced by the higher–order AuNPs stack layer structure. The peak intensity is dependent on the 4bpy density in the same SERS–active structure, indicating that the correct SERS–activity can be evaluated here. To evaluate the availability of the novel electrode with higher–order layer stack nanostructure, we estimate the SERS enhancement factor (EF). The EF is defined as $EF = \frac{I_{SERS}/N_{SERS}}{I_{NR}/N_{NR}}$, where I_{SERS} and N_{SERS} are the intensity of the SERS signal and the number of molecules contributing to I_{SERS}, respectively.[37] I_{NR} is the intensity from the normal Raman signal at the same wavenumber at which I_{SERS} is estimated. N_{NR} is the number of molecules contributing to I_{NR}. The ratio $\frac{N_{SERS}}{N_{NR}}$ is given by $\frac{N_{SERS}}{N_{NR}} = \frac{N_A \times C_{SERS}}{N_A \times C_{NR}} \times \frac{V_{SERS}}{V_{NR}}$. Here, N_A is the Avogadro number, C is the concentration of 4bpy ($C_{SERS} = 100\,nM$ and $C_{NR} = 10\,mM$), and V_{SERS} and V_{NR}

are the total volume of the laser spot. In this study, V_{SERS} is equal to V_{NR}. I_{SERS} and

I_{NR} of 100 nM and 10 mM at 1582 cm^{-1} are 483 and 45, respectively. As a result, the

EF is estimated to be ~ 1.0×10^6 with the fabricated platform using the simple Raman

spectrometer without any microscope.

The SERS enhancement factor is simply estimated to be approximately 10^6,

considering that the detection limit of normal usage without the SERS enhancement

structure is 10 mM in the simple Raman spectrometer RAM–100S with no microscope.

The other electrodes formed under the conditions #9 and #21 enabled us to detect 100

nM 4bpy (data not shown). Thus, we succeeded in obtaining a novel electrode with the

SERS–active higher–order layer stack nanostructure consisting of AuNPs. We also

found that 100 μM of 4bpy was able to be detected by the pearl chain structure (data not

shown). The higher-order nanostructure has an advantage of SERS enhancement

compared with the pearl chain structure. This is attributable to that the higher-order

layer stack gold nanostructure has more numbers of SERS–active hot site under the

field of the Raman spectrometer without microscope (field is about 2 mm $\times$ 2 mm)

than the pearl chain structure. In addition, the novel electrode with the higher–order

layer stack nanostructure provides a clue to enhancing the performance of surface–

engineered nanomaterials[38] and photothermal films for solar thermoelectric

conversion.[39)]

V. Conclusion

We fabricated a novel electrode with sterically bulky three–dimensional Au layer stack

nanostructure through the combination of convective phenomena and dielectrophoresis.

The essence of the higher–order nanostructure formation process can be explained by

the competition between five contributions: radial flow, Marangoni recirculating flow,

movement of particles towards the substrate driven by DLVO interactions,

sedimentation force and dielectrophoresis. The electrode under conditions which can

form the higher–order nanostructure enabled us to detect concentrations as low as below

100 nM 4bpy using a simple Raman spectrometer without a microscope. The SERS

enhancement factor was estimated to be approximately 10^6 times, compared to the case

without any higher–order nanostructure. Thus, the novel electrode with the SERS–

active higher–order nanostructure consisting of AuNPs will allow for measurement of

dynamic signals from biological molecules as well as environmental and chemical

reaction processes.

Acknowledgements

Correspondence and requests for materials should be addressed to A. Y.

References

1) M. G. Albrecht and J. A. Creighton, *J. Am. Chem. Soc.*, 1977, **99**, 5215 – 5217.

2) D. L. Jeanmaire and R. P. van Duyne, *J. Electroanal. Chem.* 1977, **84**, 1 – 20.

3) S. M. Nie and S. R. Emory, *Science* 1997, **275**, 1102 – 1106.

4) K. Kneipp, Y. Wang, H. Kneipp, L. T. Perelman, I. Itzkan, R. R. Dasari and M. S.

Feld,

Phys. Rev. Lett., 1997, **78**, 1667 – 1670.

5) J. B. Jackson, S. L. Westcott, L. R. Hirsh, J. L. West and N. J. Halas, *Appl. Phys. Lett.*

2003, **82**, 257 – 259.

6) K. –C. Ho, P. –J. Tsai, Y. –S. Lin and Y. –C. Chen, Anal. Chem. 2004, **76**, 7162-7168.

7) S. W. Bishnoi, Y. J. Lin, M. Tibudan, Y. Huang, M. Nakaema, V. Swarup and T. A.

Keiderling, *Anal. Chem.,* 2011, **83**, 4053 – 4060.

8) K. E. Peceros, X. Xu, S. R. Bulcock and M. B. Cortie, *J. Phys. Chem.,* 2005, **109**, 21516 – 21520.

9) W. Shi, Y. Sahoo, M. T. Swihart and P. N. Prasad, *Langmuir,* 2005, **21**, 1610 – 1617.

10) T. Kondo, K. Nishio and H. Masuda, *Appl. Phys. Exp.* 2009, **2**, 032001–1 – 032001–3.

11) S. Akil-Jaradi, S. Jradi, J. Plain, P, -M. Adam, J. –L. Bijeon, P. Royer and R. Bachelot, *RSC Adv.,* 2012*,* **2**, 7837 – 7842.

12) K. Ikeda, S. Suzuki and K. Uosaki, *Nano Lett.*, 2011, **11**, 1716 – 1722.

13) H. Liu, L. Zhang, X. Lang, Y. Yamaguchi, H. Iwasaki, Y. Inouye, Q. Xue and M. Chen, *Sci. Rep.,* 2011, **1**, 112.

14) R. Bhardwaj, X. Fang, P. Somasundaran, D. Attinger *Langmuir*, 2010, **26**, 7833 – 7842.

15) R. Takahashi, T. Fukuoka, Y. Utsumi and A. Yamaguchi, *Jpn. J. Appl. Phys.,* 2013, **52**, 06GK12.

16) R. Hara, T. Fukuoka, R. Takahashi, Y. Utsumi and A. Yamaguchi, *RSC Adv.,* 2014, **5**, 1378 – 1384.

17) D. Mark, S. Haeberle, G. Roth, F. von Stetten R. Zengerle, *Chem. Soc. Rev.* 2010,

39, 1153 – 1182.

18) P. Yager, T. Edwards, E. Fu, K. Helton, K. Nelson, M. R. Tam, B. H. Weigl, *Nature*,

2006, **442**, 412 – 418.

19) H. Hwang, D. Han, Y. –J. Oh, Y. –K. Cho, K. –H. Jeong and J. –K. Park, *Lab. Chip,*

2011, **11**, 2518 – 2525.

20) A. F. Chrimes, K. Khoshmanesh, P. R. Stoddart, A. A. Kayani, A. Mitchell, H.

Daima, V. Bansal and K. Kalantar-zadeh, *Anal. Chem.,* 2012, **84**, 4029 – 4035.

21) S. Cherukulappurath, S. H. Lee, A. Campos, C. L. Haynes and S. –H. Oh, *Chem.*

Mater., 2014, **26**, 2445 – 2452.

22) A. Yamaguchi, R. Takahashi, T. Fukuoka, R. Hara and Y. Utsumi, *to be published.*

23) S. Sriram, M. Bhaskaran, S. Chen, S. Jayawardhana, P. R. Stoddart, J. Z. Liu, N. V.

Medhekar, K. K-. Zadeh and A. Mitchell, *J. Am. Chem. Soc.* 2012, **134**, 4646 – 4653.

24) N. T. T. Trang, T. T. Thuy, D. M. Mott, M. Koyano and S. Maenosono, *Chem. Phys.*

Lett. 2013, **574**, 94 – 99.

25) R. Hogg, T.W. Healy, D.W. Fuerstenau, *Trans. Faraday Soc.*, 1966, **62**, 1638.

26) J.N. Israelachvili, *Intermolecular and Surface Forces,* 3rd Ed., Academic Press,

London, 2011.

27) C. V. Chrysikopoulos and V. I. Syngouna, *Colloids and Surfaces B: Biointerfaces*, 2012, **92**, 74.

28) S. Bhattacharjee, M. Elimelech, M. Borkovec, *Croatica Chimca Acta*, 1998, **71**, 883.

29) H. –J. Butt, K. Graf, M. Kappl, *Physics and Chemistry of Interfaces*. Wiley-VCH GmbH & Co. KGaA.

30) A. Sze, D. Erickson, L. Ren and D. Li, *J. colloid and Interface Science*, 2003, **261**, 402.

31) L. D. Landau and E. M. Lifshitz, *Fluid Mechanics*, Pergamon, London, 3rd edn, 1966.

32) T. B. Jones, *Electromechanics of Particles,* Cambridge University Press; Cambridge, England, 1995; *IEEE Eng. Med. Bio. Mag.* 2003, **22**, 33 – 42.

33) X. –B. Wang, J. Vykoukal, F. F. Becker and P. R. Gascoyne, *Biophys. J.* 1998, **74**, 2689 – 2701.

34) Y. Huang, X. B. Wang, F. F. Becker and P. R. Gascoyne, *Biophys. J.,* 1997, **73**, 1118 – 1129.

35) P. C. Lee and D. Meisel, *J. Phys. Chem.*, 1982, **86**, 3391.

36) S. W. Joo, *Vib. Spectrosc.*, 2004, **34**, 269.

37) E. C. Le Ru, E. Blackie, M. Meyer, P. G. Etchegoin, *J. Phys. Chem. C*, 2007, **111**,

13794 – 13803.

38) S. Kawata, *in Near-Field Optics and Surface Plasmon Polaritons.* Springer, Berlin,

2001.

39) A. Kosuga, Y. Yamamoto, M. Miyai, M. Matsuzawa, Y. Nishimura, S. Hedaka, K.

Yamamoto, S. Tanaka, Y. Yamamoto, S .Tokonami and T. Iida, *Nanoscale*, 7 2015,

7580 – 7584.

Figure Captions

Figure 1 Schematic of the novel electrode formation and surface–enhanced Raman

spectroscopic system.

Figure 2 Schematic of the formation process of the higher–order nanostructure. (a)

Cross–sectional cartoon of the electrodes fabricated on the glass substrate by a normal

microfabrication process consisting of a combination of UV–lithography and the lift–off

method. (b) A mixed solution of polystyrene (PS) beads and Au nanoparticles (AuNPs) is placed in the PDMS well. (c) Schematic of momentary higher–order layer stack nanostructure, including PS and AuNPs, formation through the competitive self–assembly among sedimentation, radial flow, Maragngoni flow, DLVO interactions and DEP force. Schematic images after (d) evaporation of the solution, (e) removing PS and formation of the higher–order nanostructure sustained with only AuNPs.

Figure 3 Potential energies evaluated by the DLVO theory as a function of distance (d) between (a) PS–PS, (b) PS–AuNP and (c) AuNP–AuNP in water under the assumed ion densities of 1 nM, 1 μM, 1 mM, 10 mM and 100 mM. The inset of Fig. 3(a) depicts the schematic model for DLVO interaction between the hetero particles. Forces derived from the gradient of DLVO potentials are represented for (d) PS–PS, (e) PS–AuNP and (f) AuNP–AuNP.

Figure 4 Potential energies evaluated by the DLVO theory as a function of height (h) in the cases of (a) AuNP–glass substrate and (b) PS–glass substrate in water under the assumption of ion densities of 1 nM, 1 μM, 1 mM, 10 mM and 100 mM. The inset of (a) depicts the schematic model for DLVO interaction between particle and substrate.

Forces derived from the gradient of DLVO potential energies are represented for (c)

AuNP–glass substrate and (d) PS–glass substrate.

Figure 5 Potential energies as a function of height (h) in the case of (a) AuNP–Au

electrode and (b) PS–Au electrode in water under the assumption of ion densities of 1

nM, 1 μM, 1 mM, 10 mM and 100 mM. Evaluated forces are shown in (c) AuNP–Au

electrode and (d) PS–Au electrode, respectively.

Figure 6 Particle radius dependency of the DEP forces for electrode widths/gaps of

50/50, 100/100 and 150 μm/150 μm.

Figure 7 (a) Schematic of the electrode before formation of the higher–order

nanostructure in a PDMS well containing a solution of PS and AuNPs. (b) Optical

photograph of the electrode after the evaporation of the solution and formation of the

higher–order layer stack nanostructure with AuNPs under condition #9. (c) SEM image

of the electrodes. (d) Highly magnified SEM image of the outer electrode and higher–

order nanostructure. The red square area shown in (c) corresponds to the SEM image

displayed in (d).

Figure 8 SEM images of the novel electrode with the formation of the higher–order

layer stack nanostructure under condition #12. The red square area shown in (a) is

magnified in (b). SEM images with high magnification for (c) the electrode and (d)

higher–order layer stack porous nanostructure.

Figure 9 (a) SEM image of the novel electrode after the formation of the higher–order

porous nanostructure under condition #21. (b) SEM image of the higher-order

nanostructure fabricated on the electrode.

Figure 10 SEM image of the pearl chain structure formed under condition #20.

Figure 11 Photoluminescence (PL) intensity spectra of Au electrode (a) with and (b)

without the higher–order AuNPs layer stack structure. In the inset of optical photograph,

(a) the red solid circle and (b) black solid circle correspond to the measurement

positions, respectively.

Figure 12 Characteristic enhanced Raman spectra of 4,4′–bipyridine (4bpy) at

concentrations of 100 μM, 100 nM, 1 nM, as well as a blank (ultrapure water with the

higher–order layer stack gold nanostructure and no analyte) using the Au electrode with

the higher–order AuNPs layer stack structure. Raman spectra of 10 mM 4bpy was

measured using the flat Au electrode without the higher–order nanostructure.

Table 1 Summary of experimental conditions.

No.	Electrode width (μm)	Frequency (kHz)	Particle number ratio(Au:PS)	**Higher-order nanostructure**	**SERS detection**
1	50	1	700 : 1	×	×
2	50	1	1000 : 1	×	×
3	50	1	1300 : 1	×	×
4	50	10	700 : 1	×	×
5	50	10	1000 : 1	×	**100 μM**
6	50	10	1300 : 1	×	×
7	50	100	700 : 1	×	**100 μM**
8	50	100	1000 : 1	×	×
9	50	100	1300 : 1	○	**100 nM**

10	100	1	700 : 1	×	×
11	100	1	1000 : 1	×	×
12	100	1	1300 : 1	○	**< 100nM**
13	100	10	700 : 1	×	×
14	100	10	1000 : 1	×	×
15	100	10	1300 : 1	×	×
16	100	100	700 : 1	×	×
17	100	100	1000 : 1	×	×
18	100	100	1300 : 1	×	**100 μM**
19	150	1	700 : 1	×	×
20	150	1	1000 : 1	×	×
21	150	1	1300 : 1	○	**100 nM**
22	150	10	700 : 1	×	×
23	150	10	1000 : 1	×	×
24	150	10	1300 : 1	×	×
25	150	100	700 : 1	×	×
26	150	100	1000 : 1	×	**100 μM**
27	150	100	1300 : 1	×	×

28
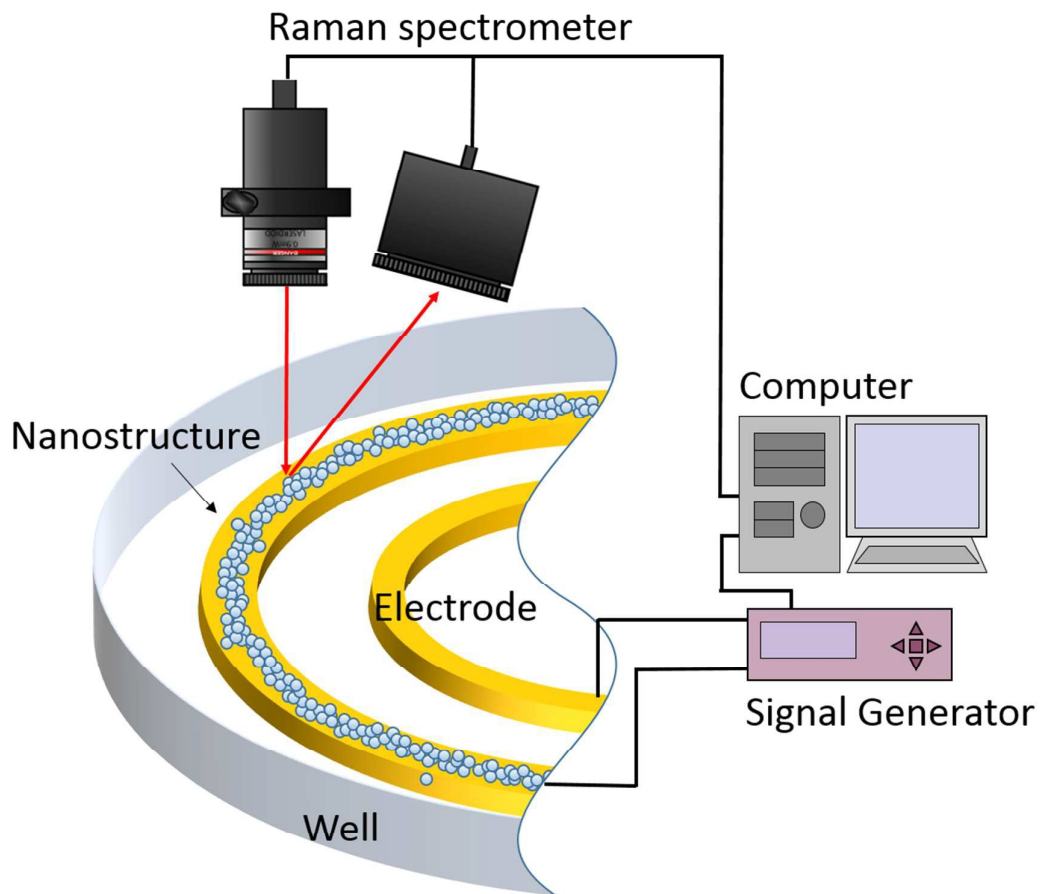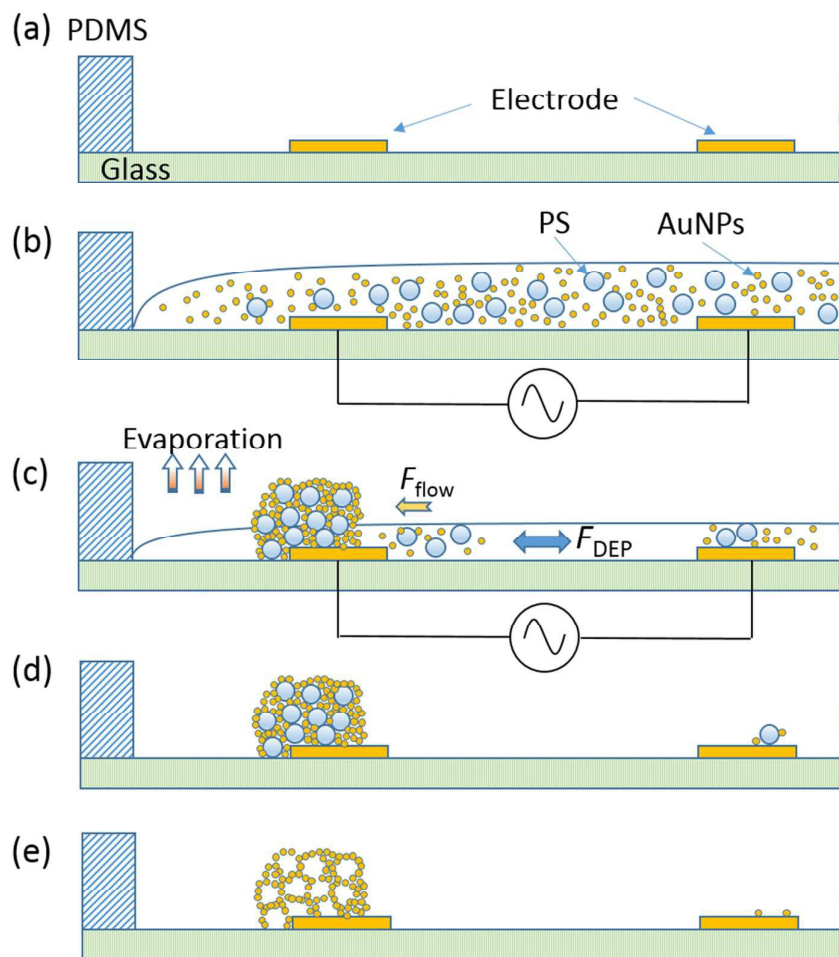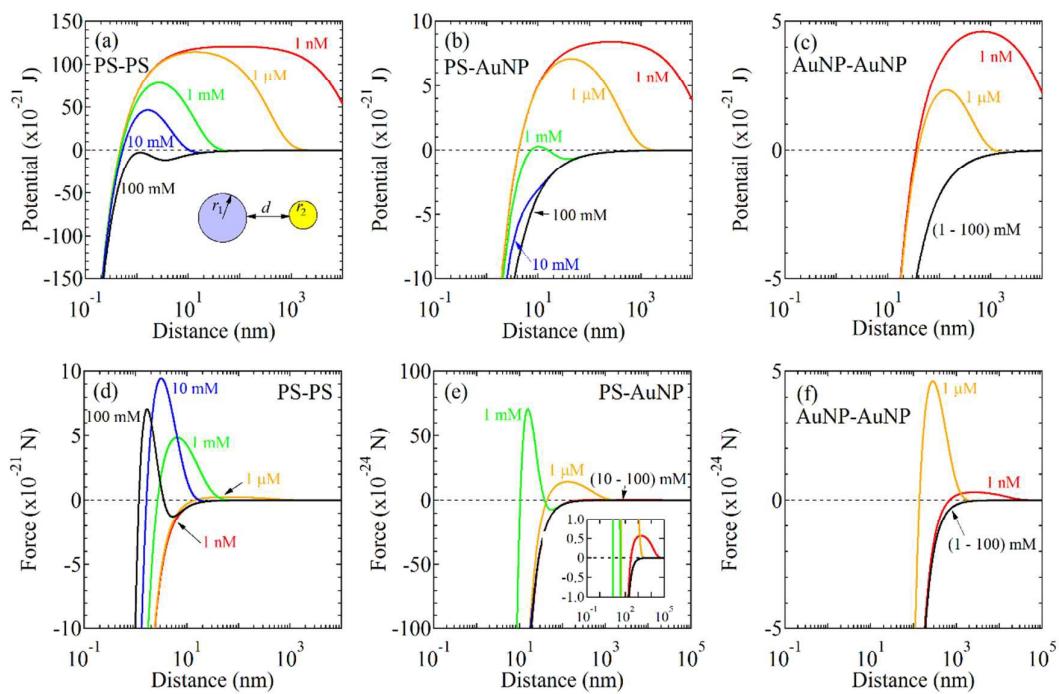
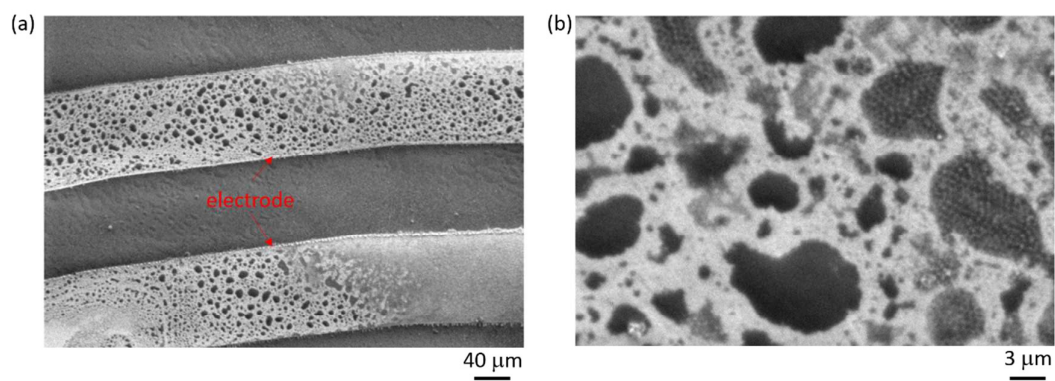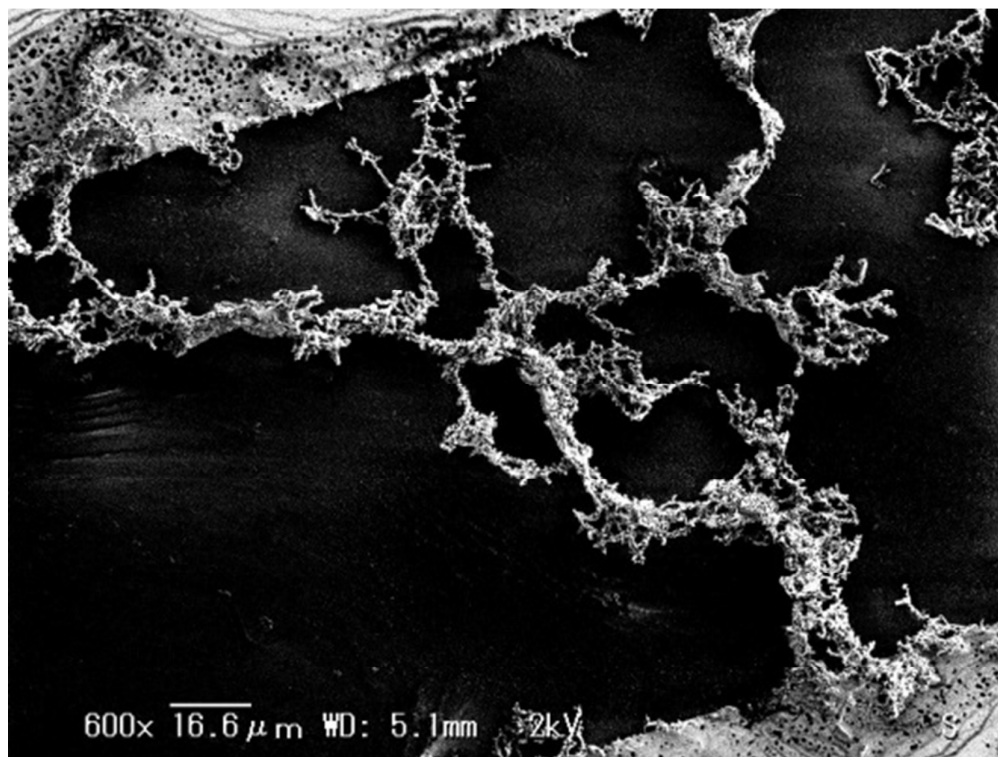Figure 1
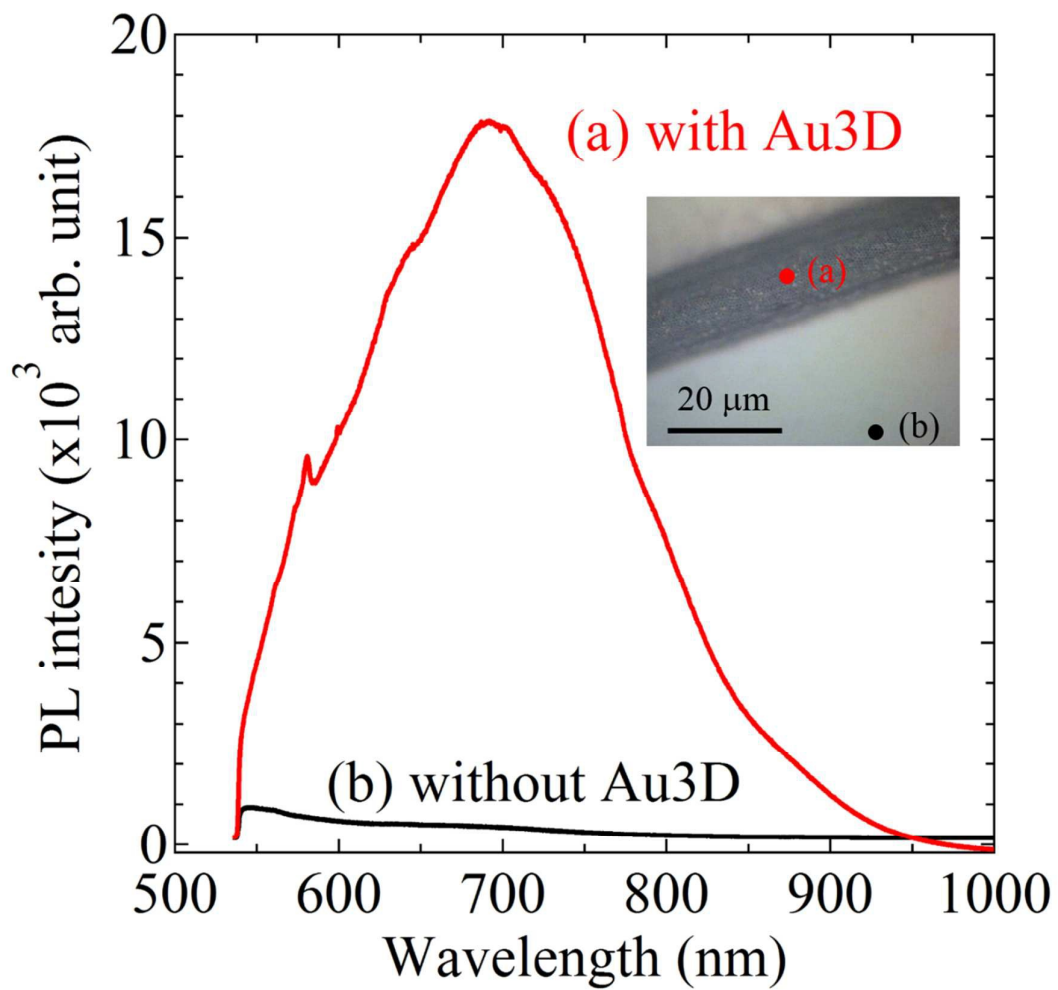
Figure 2
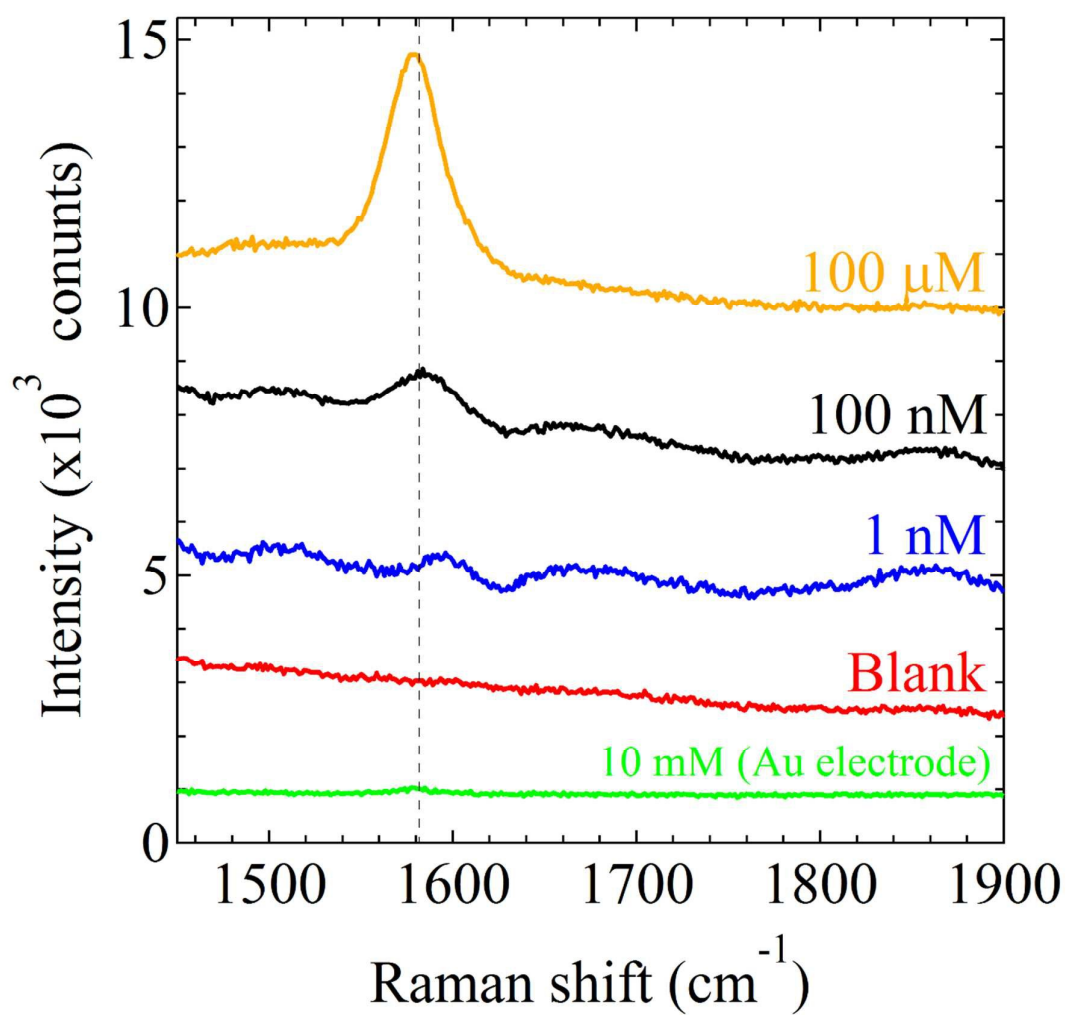
Figure 3
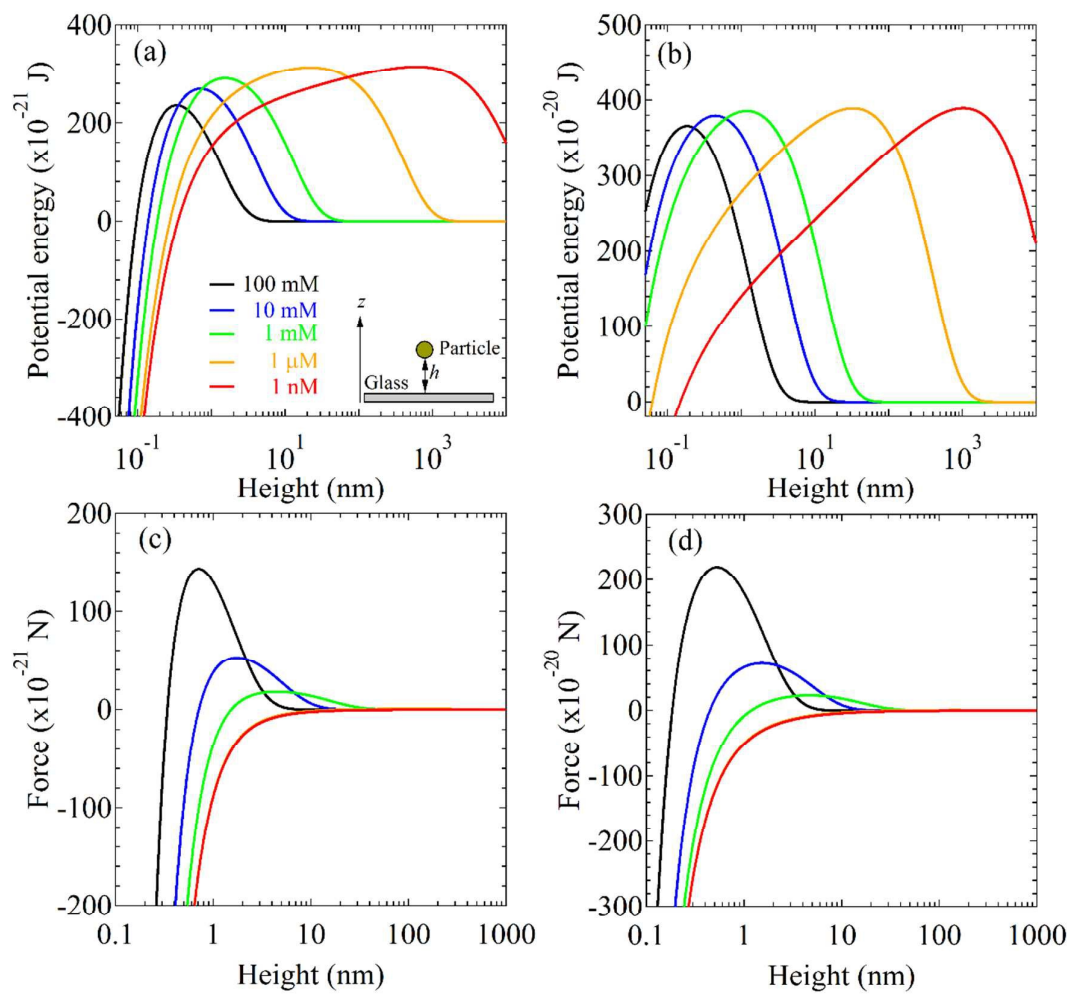
Figure 4
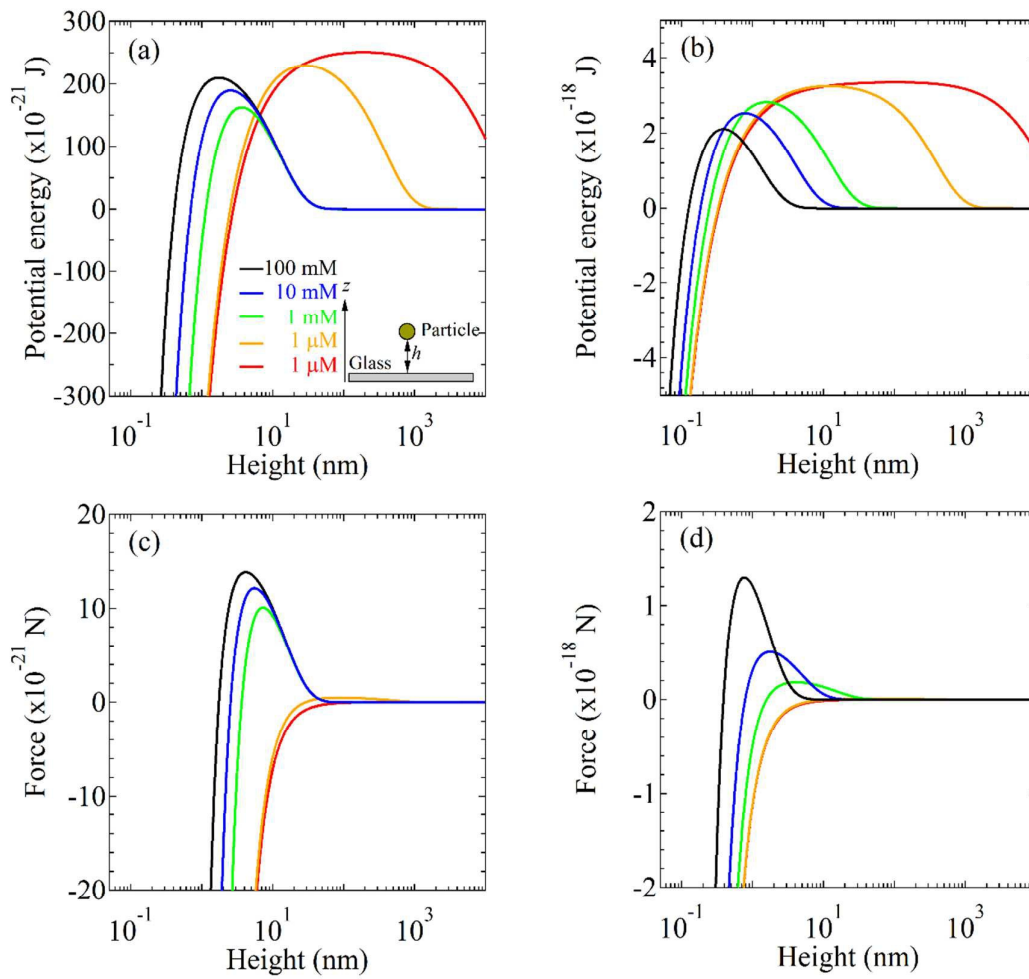
Figure 5
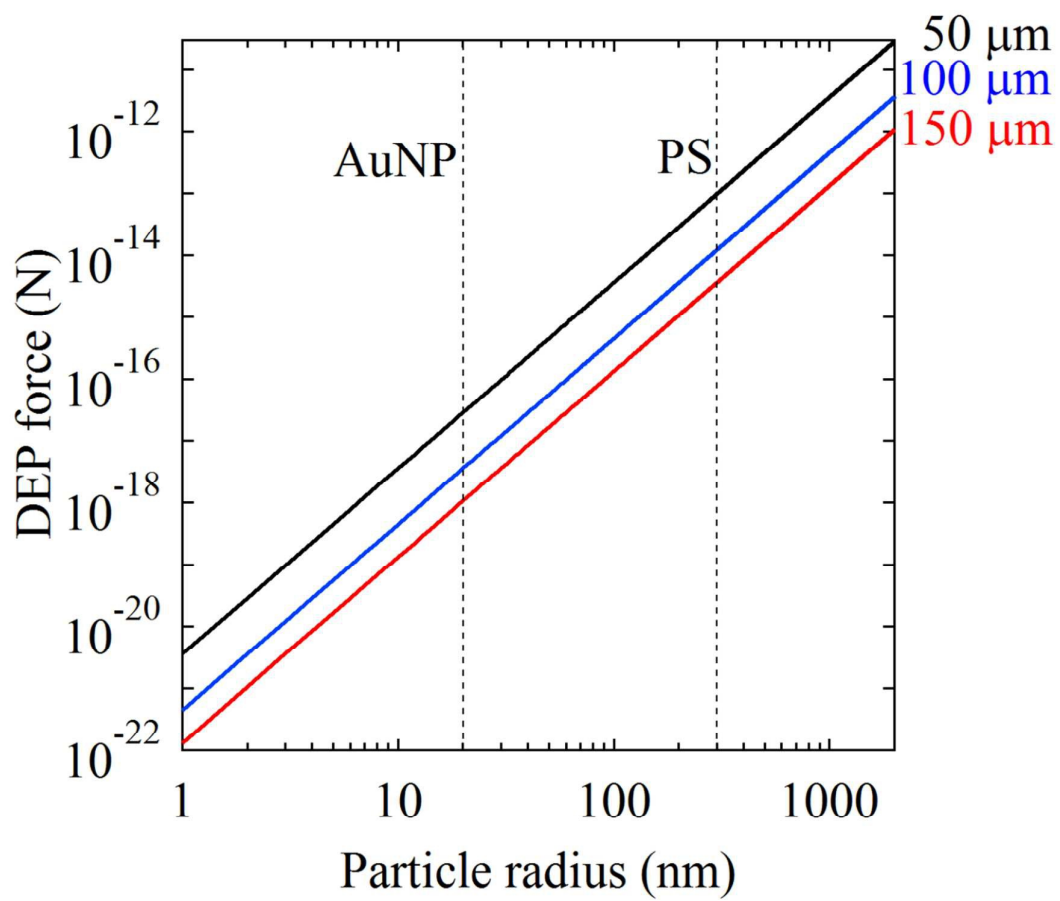
Figure 6
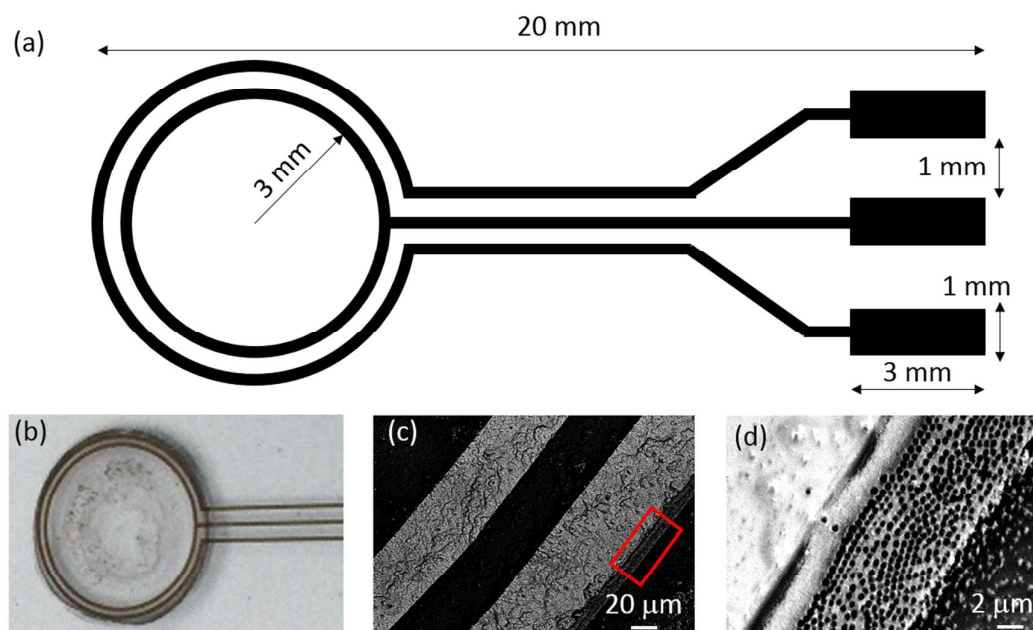
Figure 7
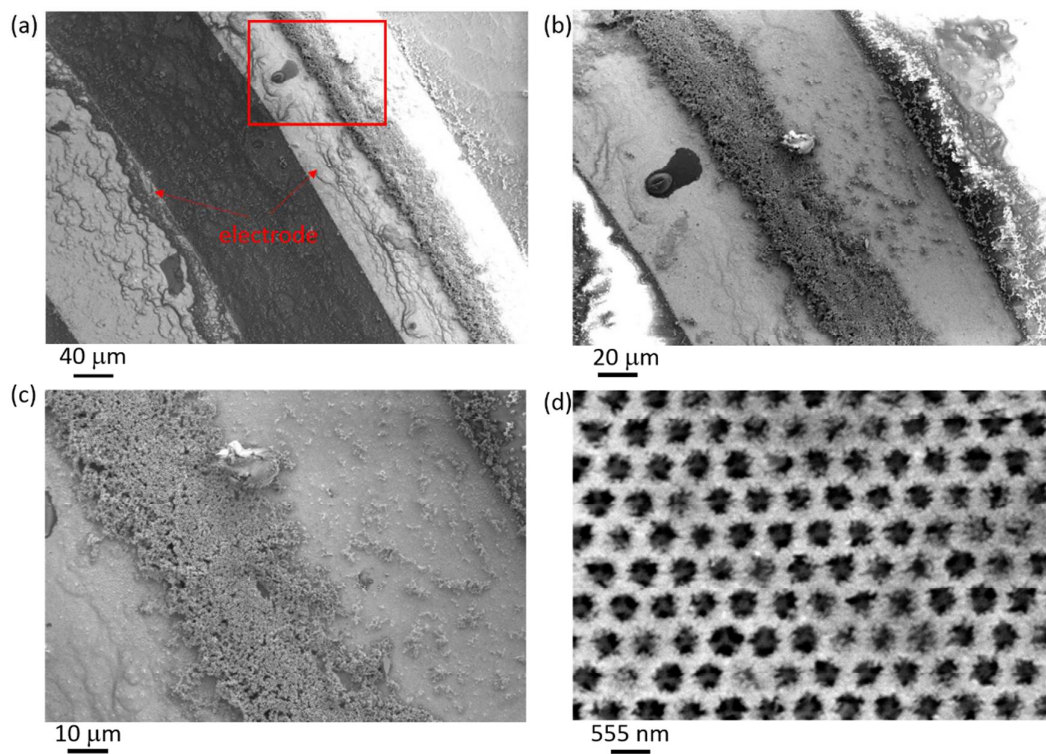
Figure 8

Figure 9

Figure 10

Figure 11

Figure 12